A numerical turbulence model for multiphase flows in the protoplanetary nebula

Joëlle M. Champney
Applied and Theoretical Mechanics, Inc., Palo Alto, California 94306

Anthony R. Dobrovolskis
University of California, Santa Cruz, California 95064

Jeffrey N. Cuzzi
NASA-Ames Research Center, Moffett Field, California 94035-1000

(Received 18 March 1994; accepted 6 March 1995)

It is thought that planets form from solid particles in a flattened, rotating, 99% gaseous nebula. These grains gradually coagulate into millimeter-to-meter sized aggregates which settle toward the midplane of the nebula. It is widely believed that the resulting dense layer eventually becomes gravitationally unstable and collapses into "planetesimals." A new numerical model is presented to simulate the predominant processes (gravitation, vertical convection, and shear-driven turbulence) during the stage while the particulate material is still dispersed about the midplane of the nebula. In our previous work, particles were assumed to be spheres of a single radius; in the present work, particles are spheres of different radii. Results indicate that neither a broad nor a narrow distribution of particle sizes is likely to become gravitationally unstable. © *1995 American Institute of Physics.*

I. INTRODUCTION

Dense regions of interstellar clouds collapse under their own gravity into young stars, surrounded by flattened disks of dusty gas.[1] Our own Solar system presumably originated from such a protoplanetary nebula. Subsequent collisions of asteroid-like "planetesimals" (followed by hydrodynamic capture of gas in the outer Solar nebula) led to their accretion into planets.

The solid component of the nebula initially consisted of microscopic grains well-mixed with the gas. These grains would gradually coagulate into millimeter-to-meter-sized aggregates, which then settle into a thin layer at the central plane of the disk due to the vertical component of the Sun's gravity.[2,3] It is widely believed[4,5] that as its density increases, this layer eventually grows gravitationally unstable and collapses directly into planetesimals. The criterion for gravitational instability may be written as

$$\rho_p > M/(\pi R^3), \tag{1}$$

where ρ_p is the bulk density of solid particles, M is the mass of the Sun, and R is the distance from the Sun.[6]

In recent years, however, it has become clear that planetesimals must form by other means, because settling of solid particles is a self-limiting process.[2,3,7,8] A radial pressure gradient causes the gaseous disk to rotate at slightly less than the Kepler orbital velocity. In contrast, the particle-rich layer is not supported by pressure, and so trends toward Keplerian motion. The resulting shear between the particle layer and the surrounding gas generates turbulence that stirs particles back into the nebula and reduces their bulk density below the stability limit.

In order to simulate this situation, we have developed a computational fluid dynamics (CFD) model for multiphase flow in which the protoplanetary nebula is treated as a mixture of gas molecules and solid particles. The temporal and spatial evolution of the mixture is described by the Reynolds-averaged Navier–Stokes equations for each phase. The gas eddy viscosity is obtained from a Prandtl turbulence model adapted to the nebula flows of interest. The particle diffusivity is modeled by means of a Schmidt number expressed as a function of particle size and density.

Our initial results, presented in Cuzzi *et al.*,[8] confirm that particles of a given mass and radius settle into a stable distribution about the midplane. In general, the lighter the particles, the thicker the layer. An interesting loophole remains, though. If particles of different sizes coexist, it is possible that the lighter particles may spread into such a thick layer that shear is reduced and turbulence is suppressed. Then the heavier particles could settle into a dense sublayer, which might become gravitationally unstable after all.

The goal of the present work is to examine this possibility by including particles of different sizes and compositions simultaneously. Our mathematical model is described in Sec. II, divided into six subsections detailing our assumptions, the model nebula, the governing equations, the perturbation technique, the Reynolds averaging method, and the turbulence model used to close the system. Section III describes the numerical technique, while Sec. IV presents the results.

II. MATHEMATICAL MODEL

A. Assumptions

The assumptions used in modeling the protoplanetary nebula are outlined below. The gas phase is assumed to be a perfect gas, known to be predominantly hydrogen. The solid phases are each assumed to consist of spherical particles of a fixed mass and radius. Each phase is treated as a continuum. Momentum is exchanged between the gas and particle phases by means of the drag force. Each particle phase is independent of the other particle phases; they interact only through the intermediary of the gas phase. The settling of

 1070-6631/95/7(7)/1703/9/$6.00

particles is modeled by taking into account turbulence generated in the gas by the presence of the particles. Collisions among particles are not taken into account, so the model is valid only for dilute suspensions; however, it contains no limitation on the mass loading ratio. The mean flow is assumed axisymmetric ($\partial/\partial\theta=0$) and isothermal. Brownian effects on the particle phase are neglected, as well as electromagnetic forces. The self-gravity of the nebula is also neglected. Cuzzi *et al.*[8] demonstrate that this assumption is valid as long as condition (1) is not close to being satisfied.

B. Nebula model

The physical characteristics of the protoplanetary nebula are now introduced. A standard "minimum mass" circumstellar nebula is assumed with total mass 0.0425 $M_\odot$. The surface mass density $\sigma(r)$ of the disk is of the form

$$\sigma(r)=\sigma_0(r/\mathrm{AU})^{-1.5}, \tag{2}$$

where AU represents 1 astronomical unit (1.49×10^{13} cm). This leads to a surface mass density $\sigma_0\approx1700$ g cm^{-2} at $r=1$ AU.

The disk is also assumed vertically isothermal at temperature

$$T(r)=T_0(r/\mathrm{AU})^{-0.5}, \tag{3}$$

where $T_0\approx280$ K. Because this is too warm for water ice to precipitate, the condensible mass fraction of 5.3×10^{-3} gives the solid particles a surface mass density of about 9 g cm^{-2} at 1 AU.

Equations (2) and (3) above imply a gas density

$$\rho_g(r,z)=\rho_{\mathrm{ref}}(r/\mathrm{AU})^{-11/4}\exp[-(z/z_G)^2], \tag{4}$$

where z_G is called the scale height. Note z_G is always much greater than the depth of the particle layer, so the variation of gas density with height can be neglected. For example, $z_G\approx8\times10^6$ km at $r=1$ AU in the baseline model. The gas density ρ_{ref} at 1 AU is 1.4×10^{-9} g cm^{-3}. The corresponding molecular mean free path is about 1 cm, so most of the particles are in the Stokes drag regime.

C. Governing equations

The equations describing the Solar nebula are expressed in a cylindrical coordinate system (r,θ,z) as
Gas phase:

$$\frac{\partial}{\partial t}\rho_g+\frac{1}{r}\frac{\partial}{\partial r}(r\rho_g u_g)+\frac{\partial}{\partial z}(\rho_g w_g)=0, \tag{5}$$

$$\frac{\partial}{\partial t}u_g+u_g\frac{\partial}{\partial r}u_g+w_g\frac{\partial}{\partial z}u_g+\frac{1}{\rho_g}\frac{\partial P}{\partial r}=\frac{v^2}{r}-\frac{GM}{R^3}r-\sum_{p=1}^{n}A_p\rho_p(u_g-u_p)+\frac{1}{\rho_g r}\frac{\partial}{\partial r}(r\tau_{rr})-\frac{\tau_{\theta\theta}}{\rho_g r}+\frac{1}{\rho_g}\frac{\partial\tau_{zr}}{\partial z}, \tag{6}$$

$$\frac{\partial}{\partial t}v_g+u_g\frac{\partial}{\partial r}v_g+w_g\frac{\partial}{\partial z}v_g=\frac{-u_g v_g}{r}-\sum_{p=1}^{n}A_p\rho_p(v_g-v_p)+\frac{1}{\rho_g r}\frac{\partial}{\partial r}(r\tau_{r\theta})+\frac{\tau_{r\theta}}{\rho_g r}+\frac{1}{\rho_g}\frac{\partial\tau_{z\theta}}{\partial z}, \tag{7}$$

$$\frac{\partial}{\partial t}w_g+u_g\frac{\partial}{\partial r}w_g+w_g\frac{\partial}{\partial z}w_g+\frac{1}{\rho_g}\frac{\partial P}{\partial z}=-\frac{GM}{R^3}z-\sum_{p=1}^{n}A_p\rho_p(w_g-w_p)+\frac{1}{\rho_g r}\frac{\partial}{\partial r}(r\tau_{zr})+\frac{1}{\rho_g}\frac{\partial\tau_{zz}}{\partial z}. \tag{8}$$

Particle phase:

$$\frac{\partial}{\partial t}\rho_p+\frac{1}{r}\frac{\partial}{\partial r}(r\rho_p u_p)+\frac{\partial}{\partial z}(\rho_p w_p)=0, \tag{9}$$

$$\frac{\partial}{\partial t}u_p+u_p\frac{\partial}{\partial r}u_p+w_p\frac{\partial}{\partial z}u_p=\frac{v_p^2}{r}-\frac{GM}{R^3}r-A_p\rho_g(u_p-u_g), \tag{10}$$

$$\frac{\partial}{\partial t}v_p+u_p\frac{\partial}{\partial r}v_p+w_p\frac{\partial}{\partial z}v_p=-\frac{u_p v_p}{r}-A_p\rho_g(v_p-v_g), \tag{11}$$

$$\frac{\partial}{\partial t}(\rho_p w_p)+\frac{1}{r}\frac{\partial}{\partial r}(r\rho_p u_p w_p)+\frac{\partial}{\partial z}(\rho_p w_p^2)=-\rho_p\frac{GM}{R^3}z-A_p\rho_g\rho_p(w_p-w_g), \tag{12}$$

where t is time, ρ is density, and P is pressure. Here u, v, and w are respectively the components of velocity in the r (radial), θ (circumferential), and z (vertical) directions. The subscripts g and p refer to the gas phase and particle phases, respectively. Here n is the number of distinct particle sizes; n is limited only by available computer resources; G is the gravitational constant, equal to 6.7×10^{-8} cm^3 g^{-1} s^{-2}. Thus the vertical and radial components of the Sun's gravitational attraction become GMz/R^3 and GMr/R^3, respectively. Finally τ_{ij} is the molecular stress tensor expressed in cylindrical coordinates, equal to $\tau_{ij}=\mu(u_{i,j}+u_{j,i})$ where $\mu=0.001$ g/cm/s is the gas molecular viscosity. Equation (12) is presented in conservative form for reasons given in Sec. III.

The drag coefficient can be expressed as $A_p=(\rho_g t_p)^{-1}$ (Ref.8), where t_p is the particle response time and depends on the ratio of the particle radius r_p to the mean free path λ_g of a gas molecule. For $r_p\leq\frac{9}{4}\lambda_g$ (Epstein flow regime),

$$t_p=\frac{\rho_s}{\rho_g}\frac{r_p}{c}. \tag{13}$$

Here ρ_s is the density of an individual solid particle, and c is the speed of sound in the gas. For $r_p>\frac{9}{4}\lambda_g$ (Stokes flow regime),

$$t_p=\frac{8}{3}\frac{\rho_s}{\rho_g}\frac{r_p}{C_D|\mathbf{v}_p-\mathbf{v}_g|}, \tag{14}$$

where C_D is the drag coefficient:

$$C_D=24\ \mathrm{Re}_p^{-1} \quad \text{for } \mathrm{Re}_p<1,$$
$$C_D=24\ \mathrm{Re}_p^{-0.6} \quad \text{for } 1<\mathrm{Re}_p<800, \tag{15}$$
$$C_D=0.44 \quad \text{for } \mathrm{Re}_p>800.$$

Here Re_p is the Reynolds number

$$\mathrm{Re}_p=\frac{2\rho_g r_p}{\mu|\mathbf{v}_p-\mathbf{v}_g|}, \tag{16}$$

where $|\mathbf{v}_p-\mathbf{v}_g|$ is the magnitude of the relative velocity between the particle phase and the gas.

D. Perturbation technique

Because we are interested in relatively small variations of physical quantities over large distance ranges, it is appropriate to solve the preceding set of equations in a perturbed form. The equations are expanded about a reference state as shown below. We seek a solution such that: $u_g=u_1$, $v_g=v_0+v_1$, $w_g=w_1$, $\rho_g=\rho_0+\rho_1$, $P=P_0+P_1$, $T=T_0$, $u_p=u_{p1}$, $v_p=v_{p0}+v_{p1}$, $w_p=w_{p1}$, $\rho_p=\rho_{p1}$.

Substitution of this expansion in the exact equations leads to the following equations at zero order:

$$\frac{\partial\rho_0}{\partial t}=0, \tag{17}$$

$$\frac{\partial P_0}{\partial r}=\frac{\rho_0 v_0^2}{r}-\frac{\rho_0 GMr}{R^3} \quad \text{(local centrifugal balance)}, \tag{18}$$

$$\frac{\partial P_0}{\partial z}=-\frac{\rho_0 GMz}{R^3} \quad \text{(hydrostatic approximation)}, \tag{19}$$

$$\frac{\partial v_0}{\partial t}=0, \tag{20}$$

$$\frac{v_{p0}^2}{r}=\frac{GMr}{R^3} \quad \text{(Keplerian motion)}. \tag{21}$$

We choose

$$P_0=\rho_0 R_g T_0/m, \quad v_{p0}=v_K, \quad v_K=r\Omega_K,$$
$$\Omega_K^2=GM/R^3, \quad v_0=v_K[1-2\eta]^{1/2},$$
$$\eta=-\frac{r}{2v_K^2}\frac{1}{\rho_0}\frac{\partial P_0}{\partial r}\ll 1. \tag{22}$$

Here R_g is the gas constant (8.3143×10^7 erg/K/mole) and m is the mean molecular weight of the gas (2.34 amu). The quantity v_K is the Keplerian orbital speed, and η is the fractional deviation of the gas from Keplerian rotation (proportional to the radial pressure gradient). To first order, the perturbed state will satisfy the following equations in their exact form:

$$\frac{\partial}{\partial t}\rho_1+\frac{1}{r}\frac{\partial}{\partial r}[r(\rho_0+\rho_1)u_1]+\frac{\partial}{\partial z}[(\rho_0+\rho_1)]w_1=0, \tag{23}$$

$$\frac{\partial}{\partial t}u_1+u_1\frac{\partial}{\partial r}u_1+w_1\frac{\partial}{\partial z}u_1$$
$$=-\frac{1}{(\rho_0+\rho_1)}\frac{\partial P_1}{\partial r}+\frac{\rho_1}{\rho_0(\rho_0+\rho_1)}\frac{\partial P_0}{\partial r}+\frac{2v_1v_0+v_1^2}{r}$$
$$+\frac{1}{(\rho_0+\rho_1)r}\frac{\partial}{\partial r}(r\tau_{rr})-\frac{\tau_{\theta\theta}}{(\rho_0+\rho_1)r}$$
$$+\frac{1}{(\rho_0+\rho_1)}\frac{\partial}{\partial z}\tau_{zr}-\sum_{p=1}^{n}A_p\rho_{p1}(u_1-u_{p1}), \tag{24}$$

$$\frac{\partial}{\partial t}v_1+u_1\frac{\partial}{\partial r}v_1+w_1\frac{\partial}{\partial z}v_1$$
$$=-u_1\frac{\partial}{\partial r}v_0-w_1\frac{\partial}{\partial z}v_0-\frac{u(v_0+v_1)}{r}$$
$$+\frac{1}{(\rho_0+\rho_1)r}\frac{\partial}{\partial r}(r\tau_{r\theta})+\frac{\tau_{r\theta}}{(\rho_0+\rho_1)r}$$
$$+\frac{1}{(\rho_0+\rho_1)}\frac{\partial}{\partial z}\tau_{z\theta}-\sum_{p=1}^{n}A_p\rho_{p1}(v_1-v_{p1}), \tag{25}$$

$$\frac{\partial}{\partial t}w_1+u_1\frac{\partial}{\partial r}w_1+w_1\frac{\partial}{\partial z}w_1$$
$$=-\frac{1}{(\rho_0+\rho_1)}\frac{\partial P_1}{\partial z}+\frac{\rho_1}{\rho_0(\rho_0+\rho_1)}\frac{\partial P_0}{\partial z}$$
$$+\frac{1}{(\rho_0+\rho_1)r}\frac{\partial}{\partial r}(r\tau_{zr})+\frac{1}{(\rho_0+\rho_1)}\frac{\partial}{\partial z}\tau_{zz}$$
$$-\sum_{p=1}^{n}A_p\rho_{p1}(w_1-w_{p1}), \tag{26}$$

$$\frac{\partial}{\partial t}\rho_{p1}+\frac{1}{r}\frac{\partial}{\partial r}(r\rho_{p1}u_{p1})+\frac{\partial}{\partial z}(\rho_{p1}w_{p1})=0, \tag{27}$$

$$\frac{\partial}{\partial t}u_{p1}+u_{p1}\frac{\partial}{\partial r}u_{p1}+w_{p1}\frac{\partial}{\partial z}u_{p1}$$
$$=\frac{v_{p1}^2+2v_{p0}v_{p1}}{r}-A_p(\rho_0+\rho_1)(u_{p1}-u_1), \tag{28}$$

$$\frac{\partial}{\partial t}v_{p1}+u_{p1}\frac{\partial}{\partial r}v_{p1}+w_{p1}\frac{\partial}{\partial z}v_{p1}$$
$$=-\frac{u_{p1}(v_{p0}+v_{p1})}{r}-u_{p1}\frac{\partial v_{p0}}{\partial r}-w_{p1}\frac{\partial v_{p0}}{\partial z}$$
$$-A_p(\rho_0+\rho_1)(v_{p0}+v_{p1}-v_0-v_1), \tag{29}$$

$$\frac{\partial}{\partial t}(\rho_p w_{p1})+\frac{1}{r}\frac{\partial}{\partial r}(r\rho_{p1}u_{p1}w_{p1})+\frac{\partial}{\partial z}(\rho_{p1}w_{p1}^2)$$
$$=-\rho_{p1}\frac{GM}{R^3}z-A_p(\rho_0+\rho_1)\rho_{p1}(w_{p1}-w_1). \tag{30}$$

E. Reynolds averaging

The perturbation quantities themselves are further expanded into means and variations, in the usual notation: $\rho_1=\bar{\rho}+\rho'$, $u_1=\bar{u}+u'$, $v_1=\bar{v}+v'$, $w_1=\bar{w}+w'$. By definition, variation quantities vanish on the average: $\overline{\rho'}=0$, $\overline{u'}=0$, $\overline{v'}=0$, $\overline{w'}=0$, etc. This form is substituted into the perturbation equations (23)–(30), which are then time averaged (Reynolds averaged) over an interval short compared to the evolution of the nebula but long compared to the time scales of the turbulence.

Originally, we solved the vertical gas momentum equation (8) for $\bar{w}$, the mean value of the gas vertical velocity perturbation. However, the Courant–Friedrichs–Lewy (CFL) condition required a very small time step for Eq. (8) to be numerically stable. We soon found that neglecting $\bar{w}$ eliminated the need for this CFL condition, and the time step could be increased an order of magnitude. Since $\bar{w}$ was always small, setting $\bar{w}=0$ made no noticeable difference in the results.

Since the gas density ρ_g is nearly constant, its fluctuation will be very small, and any correlation involving ρ_g' is neglected. In the simulations presented in this paper, radial gradients ($\partial/\partial r$) of perturbation quantities are also neglected by scaling. The resulting set of equations is shown below in the form in which they are solved. The overbar sign on all mean variables has been eliminated for clarity;

$$\frac{\partial}{\partial t}\rho+\frac{\partial}{\partial z}[(\rho_0+\rho)w]=0, \tag{31}$$

$$\frac{\partial u}{\partial t}+w\frac{\partial u}{\partial z}=\frac{\rho}{\rho_0(\rho_0+\rho)}\frac{\partial P_0}{\partial r}+\frac{2vv_0+v^2}{r}-\frac{\tau_{\theta\theta}^T}{(\rho_0+\rho)r}+\frac{1}{(\rho_0+\rho)}\frac{\partial}{\partial z}\tau_{zr}^T-\sum_{p=1}^{n}A_p\rho_p(u-u_p), \tag{32}$$

$$\frac{\partial v}{\partial t}+w\frac{\partial v}{\partial z}=-u\frac{\partial v_0}{\partial r}-w\frac{\partial v_0}{\partial z}-\frac{u(v_0+v)}{r}+\frac{\tau_{r\theta}^T}{(\rho_0+\rho)r}+\frac{1}{(\rho_0+\rho)}\frac{\partial}{\partial z}\tau_{z\theta}^T-\sum_{p=1}^{n}A_p\rho_p(v_0+v-v_{p0}-v_p), \tag{33}$$

$$w=0, \tag{34}$$

$$\frac{\partial}{\partial t}\rho_p+\frac{\partial}{\partial z}(\rho_p w_p+\overline{\rho_p' w_p'})=0, \tag{35}$$

$$\frac{\partial u_p}{\partial t}+w_p\frac{\partial u_p}{\partial z}=\frac{2v_pv_{p0}+v_p^2}{r}+\frac{\tau_{p\theta\theta}^t}{\rho_p r}+\frac{1}{\rho_p}\frac{\partial}{\partial z}\tau_{pzr}^t-\frac{\overline{\rho_p' w_p'}}{\rho_p}\frac{\partial u_p}{\partial z}-A_p(\rho_0+\rho)(u_p-u), \tag{36}$$

$$\frac{\partial v_p}{\partial t}+w_p\frac{\partial v_p}{\partial z}=-u_p\frac{\partial v_{p0}}{\partial r}-w_p\frac{\partial v_{p0}}{\partial z}-\frac{u_p(v_{p0}+v_p)}{r}+\frac{\tau_{pr\theta}^t}{\rho_p r}+\frac{1}{\rho_p}\frac{\partial}{\partial z}\tau_{pz\theta}^t-\frac{\overline{\rho_p' w_p'}}{\rho_p}\frac{\partial v_{0p}}{\partial z}-\frac{1}{\rho_p}\frac{\partial}{\partial z}(v_p\overline{\rho_p' w_p'})-A_p(\rho_0+\rho)(v_{p0}+v_p-v_0-v), \tag{37}$$

$$\frac{\partial}{\partial t}(\rho_p w_p)+\frac{\partial}{\partial z}(\rho_p w_p^2)=-\rho_p\frac{GM}{R^3}z+\frac{\partial\tau_{pzz}^t}{\partial z}-2\frac{\partial}{\partial z}(\overline{\rho_p' w_p' w_p})-A_p(\rho_0+\rho)\rho_p(w_p-w)-A_p(\rho_0+\rho)(\overline{\rho_p' w_p'}-\overline{\rho_p' w_g'}). \tag{38}$$

In the viscous stresses, the superscript t stands for turbulent, while T stands for the total of the molecular and turbulent stresses: $\tau_{ij}^t=-\rho_g\overline{u_i' u_j'}$, $\tau_{ij}^T=\tau_{ij}+\tau_{ij}^t$. The gas stresses are expressed as

$$\tau_{rr}^T=-\frac{2}{3}k,\quad \tau_{r\theta}^T=-(\mu+\mu_t)\frac{v_0+v}{r},$$
$$\tau_{rz}^T=(\mu+\mu_t)\frac{\partial u}{\partial z},\quad \tau_{\theta\theta}^T=-\frac{2}{3}k+2(\mu+\mu_t)\frac{u}{r},$$
$$\tau_{zz}^T=-\frac{2}{3}k+\frac{2}{3}(\mu+\mu_t)\frac{\partial w}{\partial z},$$
$$\tau_{z\theta}^T=(\mu+\mu_t)\frac{\partial}{\partial z}(v_0+v), \tag{39}$$

where k is the kinetic energy of the gas turbulence. The particle stresses are

$$\tau_{prr}^t=0,\quad \tau_{pr\theta}^t=-\frac{\mu_t}{S_c}\frac{v_{p0}+v_p}{r},\quad \tau_{prz}^t=\frac{\mu_t}{S_c}\frac{\partial u_p}{\partial z},$$
$$\tau_{p\theta\theta}^t=2\frac{\mu_t}{S_c}\frac{u_p}{r},\quad \tau_{pzz}^t=\frac{4}{3}\frac{\mu_t}{S_c}\frac{\partial w_p}{\partial z}, \tag{40}$$
$$\tau_{pz\theta}^t=\frac{\mu_t}{S_c}\frac{\partial}{\partial z}(v_{p0}+v_p).$$

F. Turbulence modeling

To close the system of equations, we adopted the formulation of Cuzzi *et al.*,[8] summarized as follows. Applying the Prandtl mixing length model to nebula flows, we express the turbulent eddy viscosity μ_t as the square of a mixing length times the local gas density and vorticity:

$$\mu_t=(c_v\delta)^2\rho_g\sqrt{\left(\frac{\partial u}{\partial z}\right)^2+\left(\frac{\partial v}{\partial z}\right)^2}. \tag{41}$$

Here we take the mixing length equal to a constant $c_v=0.045$ times the boundary layer thickness $\delta\approx 0.02\eta v_K/\Omega_K$.

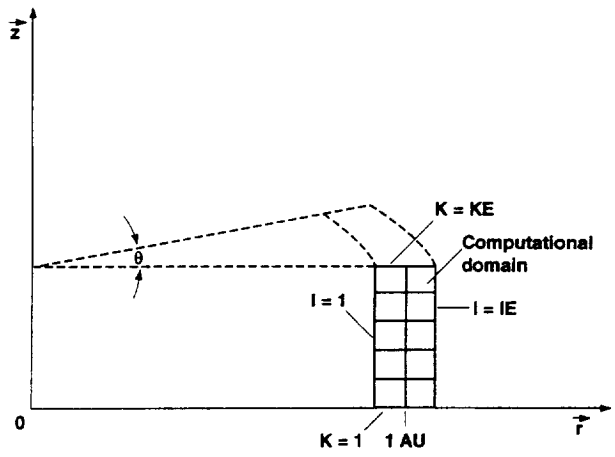

FIG. 1. Geometry of nebula flow simulations.

Correlations between particle density and particle velocity are specified according to the gradient diffusion hypothesis. Since the particle density gradient is dominated by its vertical component, this implies

$$\overline{\rho_p' u_p'}=0, \quad \overline{\rho_p' v_p'}=0, \quad \overline{\rho_p' w_p'}=-\frac{\mu_t}{S_c \rho_g}\frac{\partial}{\partial z}\overline{\rho_p}. \tag{42}$$

Here S_c is the Schmidt number, given by

$$S_c=(1+S_t)\sqrt{1+3\overline{w_p^2}\rho_g/2k}, \tag{43}$$

where $S_t=\Omega_K t_p$ is called the particle Stokes number, and $t_p\equiv(A_p\rho_g)^{-1}$ is the time constant of the drag.[8] The turbulent kinetic energy k is obtained from the eddy viscosity μ_t through the relation

$$\mu_t=\frac{C_\mu^{1/2}}{R_0}\frac{k}{\Omega_K}, \tag{44}$$

where R_0 is the critical Rossby number (empirically set to 80) and C_μ is a dimensionless coefficient (set to 0.09; Ref. 8).

Correlations between particle density and gas velocity are taken approximately equal to the corresponding particle–particle correlations. Consequently, the drag term involving the difference $(\overline{\rho_p' w_p'}-\overline{\rho_p' w_g'})$ cancels out of Eq. (38) for the vertical momentum of the particles.

III. NUMERICAL TECHNIQUE

A. Algorithm

The multiphase flow code is an extension of the two-phase flow code, with all particle variables expressed as arrays to take into account the different sizes of particles. The code employs dimensional variables, expressed in CGS units, but this can easily be changed. In this code, the time-dependent Navier–Stokes equations (31)–(38) are solved using a time-marching approach. Time-dependent methods are commonly used in Computational Fluid Dynamics applications to obtain a steady-state numerical solution of a fluid flow. By their use, a boundary-value problem is transformed into an initial-boundary value problem with unknown initial data (see Yee, Ref. 9, p. 127), for which efficient algorithms can be used.

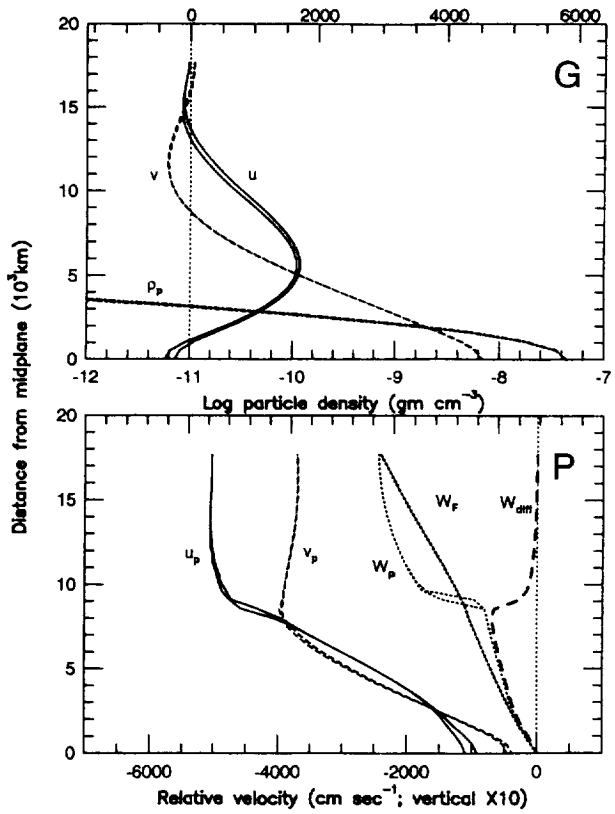

FIG. 2. Model results at 1 AU for particles 60 cm in radius after 13 years of simulated time. The upper panel (labeled "G") displays the gas velocity components u,v,w along with the particle density profile ρ_p, while the lower panel (labeled "P") shows the velocity components u_p,v_p,w_p for the particles. The diffusion velocity w_{diff} and terminal velocity w_F are defined in the text.

Implicit algorithms to solve partial differential equations with stiff source terms, like those in this paper, are still at the development stage (see Yee, Ref. 9, p. 118). Because our goal is to obtain a numerical solution to an as-yet unsolved problem, we use a well-developed explicit algorithm. We selected the 1969 MacCormack scheme,[10] because it has widely been used in aerodynamical simulations, although it has not been applied to astrophysical problems until this work.[7,8] We refer the reader to the work of Mendez-Nunez and Carroll,[11,12] who recently evaluated the MacCormack algorithm for atmospheric problems and demonstrated its advantages with respect to numerical stability, diffusion, and dispersion.

The radial and azimuthal momentum equations (32), (33), (36), and (37) are solved in nonconservative form. This form is employed instead of the more common conservative form in order to minimize roundoff errors in the particle velocities. In the conservative form, such errors may arise when the conservative variables $\rho_p u_p,\rho_p v_p,\rho_p w_p$ are divided by the density ρ_p to obtain the primitive variables u_p,v_p,w_p. With the nonconservative form, this is avoided since we solve directly for the primitive variables.

However, we encountered a problem with the particle

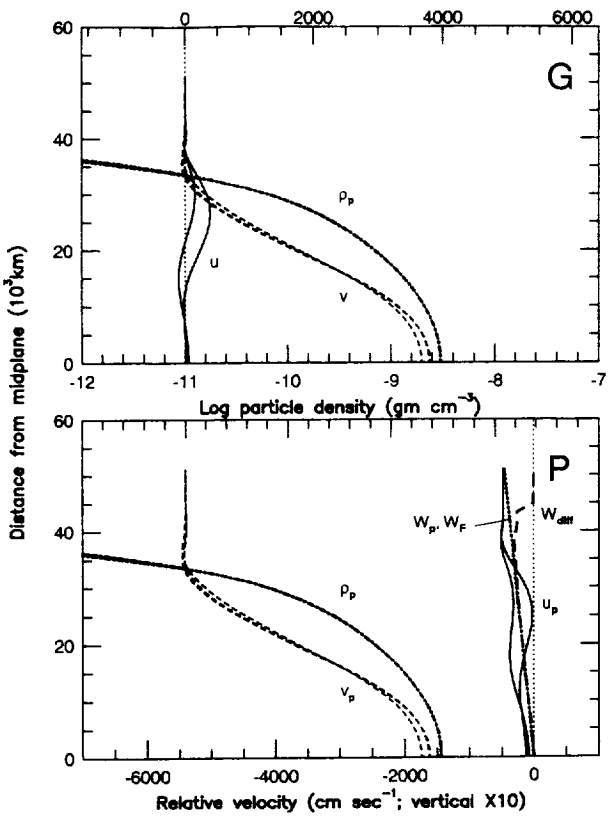

FIG. 3. Similar to Fig. 2, but all particles are 10 cm in radius. Note change in scales.

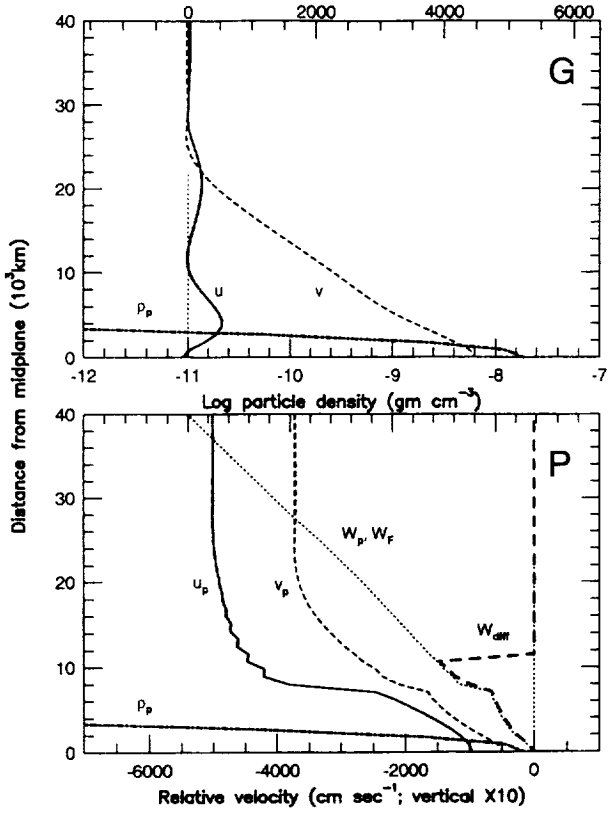

FIG. 4. Similar to Fig. 3, but for the 60 cm particles in a nebula containing equal masses of particles 10 and 60 cm in radius. Note change in scales.

vertical momentum equation. Because of the terms containing $\overline{\rho_p' w_p'}$ which originated from averaging advection terms, the conservative form (38) is actually more stable. In the one-dimensional case treated here, the particle continuity equation (35) and vertical momentum equation (38) are strongly coupled to each other, but coupled to the other two particle momentum equations (36) and (37) only through the value of the turbulent viscosity μ_t. Because of this situation, we have adopted a hybrid solution scheme. We solve (35) and (38) simultaneously in conservative form using first-order, upwind differencing for the advective terms (sacrificing some accuracy for the sake of stability), and second-order central differencing for the viscous terms. Then ρ_p and w_p are updated to the next time step, and the gas and particle radial and azimuthal momentum equations are solved in nonconservative form.

Although this approach was stable, the algorithm tended to lose particle mass, due to excessive numerical diffusion arising from the first-order spatial differencing. Sophisticated numerical techniques that conserve particle (or species) mass to machine accuracy have been designed for unsteady multidimensional aerosol problems, in particular by Toon *et al.*[13] However, because we are looking for the steady-state solution, a simpler approach was employed to conserve particle mass.

We periodically applied an integrodifferential correction to compensate for the loss of particle mass. In a steady state, $\partial \rho_p / \partial t = 0$, so that the particle continuity equation (35) and formula (42) give

$$\bar{\rho}_p \bar{w}_p + \overline{\rho_p' w_p'} = C = \bar{\rho}_p \bar{w}_p - \frac{\mu_t}{S_c \rho_g} \frac{\partial \rho_p}{\partial z}, \tag{45}$$

where C is a constant. Evaluating the left side of Eq. (45) above at $z=0$ gives $C=0$, while integrating it leads to

$$\bar{\rho}_p(z) = \bar{\rho}_p(0) \exp\left(\int_0^z \frac{S_c \rho_g}{\mu_t} \bar{w}_p \, dz \right). \tag{46}$$

In the numerical model, the value of $\bar{\rho}_p(0)$ is determined from the total initial particle mass, and the profile of $\bar{\rho}_p(z)$ is updated at each time step from Eq. (46) above. This technique was found to be quite successful.

B. Boundary conditions

Our code was designed to treat flow in both the vertical and radial directions. Because so little is known about the particle settling, though, we have thus far restricted ourselves to one-dimensional calculations. Since the largest gradients lie in the vertical direction, we have neglected the complication of radial flow for the time being. Accordingly, we define the numerical grid with either 102 or 202 rows in the vertical direction, but only three columns (IE=3) in the radial direction. This geometry is depicted in Fig. 1. Zero-gradient conditions are imposed at both radial boundaries $I=1$ and $I=3$, so that all dependent variables are the same in each vertical column. Similar conditions are imposed on the horizontal rows $K=1$ and $K=3$, corresponding to symmetry across the midplane at $K=2$.

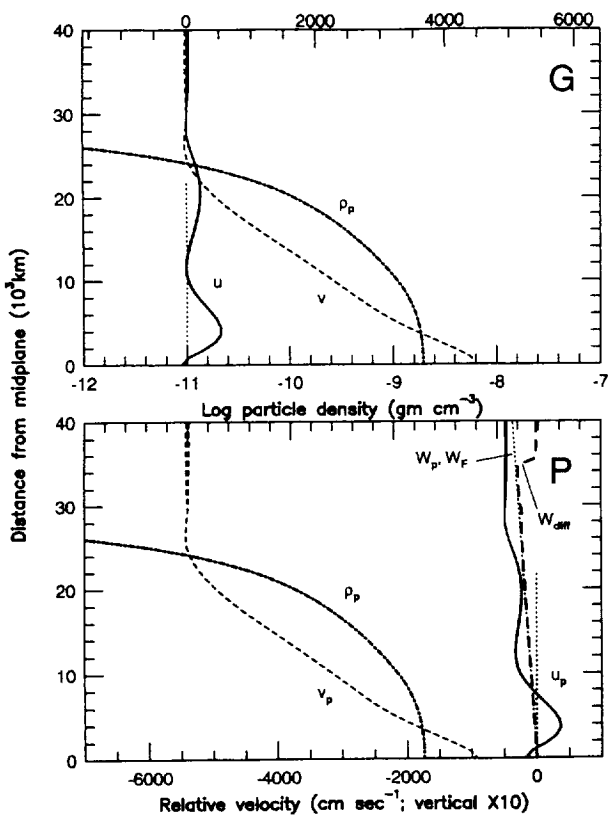

FIG. 5. Similar to Fig. 4, but for the 10 cm particles in a nebula containing equal masses of particles 10 and 60 cm in radius.

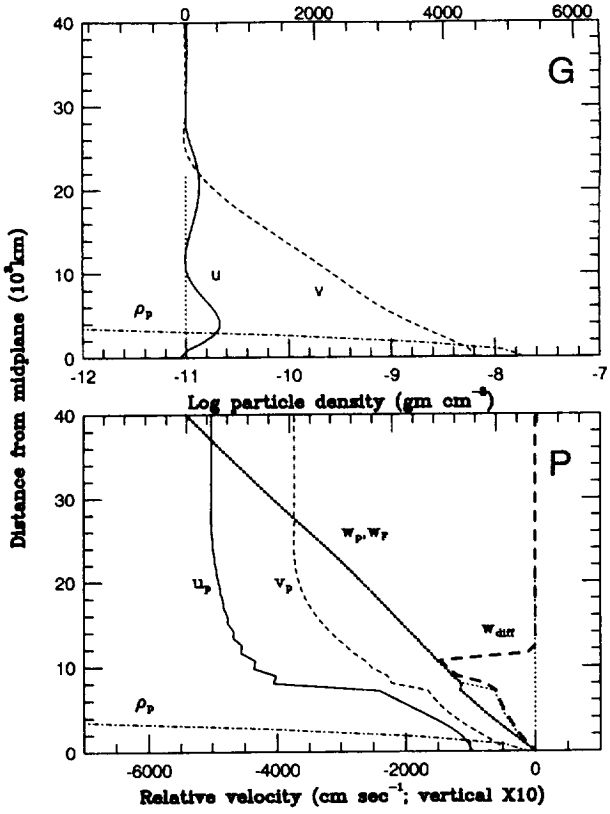

FIG. 6. Similar to Fig. 4, but after 51 years of simulated time.

For the upper boundary conditions, we adapted the approximate analytic solution of Nakagawa *et al.*[14] They were modeling a simple two-phase nebula, but we extended their results to multiple particle sizes. The results imply that as the particle density approaches zero far from the midplane, the density and velocity variations of the gas also vanish. In contrast, the particle velocity variations approach the limits

$$u_p=\frac{-2v_K S_t}{1+S_t^2},\quad v_p=\frac{-\eta v_K}{1+S_t^2},\quad w_p=-z\Omega_K S_t. \tag{47}$$

We therefore imposed the above conditions on the density and velocity variations of each phase at the upper boundary $K=KE$.

C. Code verification

The nature of nebula flows does not permit direct comparisons of simulations with experiment. Instead, computations were verified by means of "internal" checks. First, a trivial test was performed. The new multiphase code was compared to our "old" two-phase flow code[8] for a mixture of gas with particles of a single size. Results for the two cases were identical. Next, these were compared to a multiphase computation with all particles again of the same size, but now treated as two separate phases. The mass of each particle phase was half the mass of particles in the two-phase flow run. The results were still unchanged, as expected.

IV. RESULTS

Our first results are described below. The flow is a mixture of solid particles of individual density $\rho_s=1.0$ g/cm^3 with nebular gas at $r=1$ AU where the temperature is 280 K. Initially, the mesh consisted of 102 points with a vertical resolution of 600 km and a time step of 1/2 hour. After 11 years of evolution, the mesh was refined by linear interpolation to 202 points with a vertical resolution of 300 km, and restarted with a time step of 1/4 hour. This resolution is still ~100 times larger than the smallest eddies, and the time step is orders of 10 longer than their turnover time. In each case, the multiphase flow runs extend over about 13 years of simulated time, requiring about 2 hours of CPU time on a Cray Y-MP. Over the duration of the runs, residuals dropped by more than 4 orders of magnitude, indicating good convergence toward a steady-state solution.

The results of these simulations are shown in Figs. 2–4. Figure 2 represents a two-phase run in which all particles were 60 cm in radius, while Fig. 3 displays a similar case where all particles were 10 cm in radius. These cases were selected because of the contrast in the thickness of the particle layers. For comparison, Figs. 4 and 5 present a multiphase flow containing equal masses of both species; Fig. 4 refers to the particles of radius 60 cm while Fig. 5 applies to those of radius 10 cm. The total mass of all particles was the same in every run.

The dot–dashed curves in each figure plot the bulk density ρ_p of the particle cloud; the scale is shown at the bottom of the upper panel. The solid and dashed curves in the lower

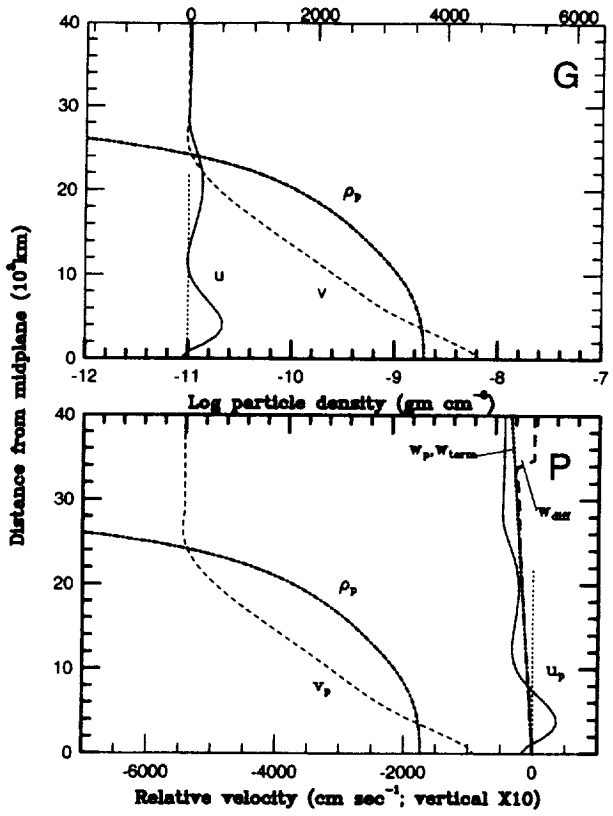

FIG. 7. Similar to Fig. 5, but after 51 years of simulated time.

panel (labeled "P") respectively show the radial and azimuthal components u_p and v_p of the particle velocity, measured with respect to the Keplerian speed v_K (bottom scale). The corresponding gas velocities u and v are shown in the upper panel (labeled "G"), relative to pressure-supported circular motion v_0 (top scale).

The light dotted line in the lower panel represents the particle vertical velocity w_p. The heavy dashed curve is the diffusion velocity

$$w_{\text{diff}} \equiv -\overline{\rho_p' w_p'}/\overline{\rho_p} = \frac{\mu_T}{S_c \rho_g}\frac{1}{\overline{\rho_p}}\frac{\partial}{\partial z}\overline{\rho_p}, \tag{48}$$

defined as the effective velocity of the mass flow driven by the particle density gradient.[8] The good agreement between w_{diff} and w_p in the dense particle layer indicates that the particles are not settling appreciably.

The heavy dotted curve plots the terminal velocity w_F, the speed of fall for which the particle's weight is balanced by drag:

$$w_F = -\frac{GM}{R^3}\frac{z}{A\rho_0} = -\Omega_K^2 z t_p(z). \tag{49}$$

For the 60 cm particles of Figs. 2 and 4, w_F differs from w_p because particles falling from higher levels retain some momentum. In contrast, w_F is indistinguishable from w_p for the 10 cm particles of Figs. 3 and 5, indicating that the falling speed of the small particles continually adjusts to the local terminal velocity.

Note that the particle density profile ρ_p is much thicker in the 10 cm case (Fig. 3) than in the 60 cm run (Fig. 2). This is due to the greater diffusivity of the smaller particles. As a result, the profiles of azimuthal velocity v and v_p are also thicker in Fig. 3 than in Fig. 2. Overall, the results of the multiphase calculations (Figs. 4 and 5) are fairly similar to the results of the two-phase runs (Figs. 2 and 3). As expected, the velocity gradient in the multiphase case is intermediate between that in the two unimodal cases. This actually causes the 10 cm particles in Fig. 5 to settle into a thinner layer than in Fig. 3. However, the distribution of 60 cm particles in Fig. 4 is no denser than that in Fig. 2. This indicates that more realistic models including a broad distribution of particle sizes are not likely to be less stable in the Goldreich–Ward sense.[5]

In Fig. 4, we also observe numerical oscillations in the radial velocity u_p of the 60 cm particles that were not present in the two-phase flow computations. We verified that these oscillations are reduced with a finer mesh, confirming that they are of numerical origin, and caused by our unwillingness to use an artificial viscosity.

Note in each figure that drag between the particle-rich layer and the surrounding particle-poor nebula causes a radial outflow of the gas. This outflow u peaks at ~5,000 km above the midplane in Fig. 2, and at ~30 000 km in Fig. 3, just above the respective particle-rich layers. In the multiphase case, however, we observe two maxima in u corresponding to both particle sublayers. This effect could have significant implications for the radial transport of small particles in the protoplanetary nebula and the compositional inhomogeneity of planetesimals.

Finally, we extended the multiphase run from 13 years to 51 years of simulated time. Lack of time and resources prevented our optimizing the time step, so we simply increased it by a factor of 10 and restarted the run. The results, displayed in Figs. 6 and 7, are practically indistinguishable from those at 13 years plotted in Figs. 4 and 5. This demonstrates that a steady state has indeed been reached.

ACKNOWLEDGMENTS

The first author dedicates this paper to the memory of her husband Philip D'Arcy Champney, who was so enthusiastic and supportive of her research endeavor. We also thank Dr. Thomas Coakley, Dr. Stuart Weidenschilling, and two anonymous referees for their comments and suggestions. Dr. Brian Toon also provided helpful suggestions and some support to complete this paper. This research was funded by NASA's Planetary Geology and Geophysics and Origins of Solar Systems programs. The Numerical Aerodynamic Simulator program of NASA's Office of Aeronautics supplied computational support.

[1] F. Shu, J. Najita, D. Galli, E. Ostriker, and S. Lizano, "The collapse of clouds and the formation and evolution ofstars and disks," in *Protostars and Planets III*, edited by E. H. Levy and J. I. Lunine (University of Arizona Press, Tuscon, AZ, 1993), pp. 3–45.

[2] S. J. Weidenschilling, "Dust to planetesimals: settling and coagulation in the solar nebula," Icarus **44**, 172 (1980).

[3] S. J. Weidenschilling and J. N. Cuzzi, "Formation of planetesimals in the solar nebula," in *Protostars and Planets III*, edited by E. H. Levy and J. I.

Lunine (University of Arizona Press, Tuscon, AZ, 1993), pp. 1031–1060.
[4]V. S. Safronov, *Evolution of the Protoplanetary Cloud and Formation of the Earth and Planets* (Israel Program for Scientific Translations, 1972).
[5]P. Goldreich and W. R. Ward, "The formation of planetesimals," Astrophys. J. **183**, 1051 (1973).
[6]A. J. Toomre, "On the gravitational stability of a disk of stars," Astrophys. J. **139**, 1217 (1964).
[7]J. M. Champney and J. N. Cuzzi, "A turbulent two-phase flow model for nebula flows," American Institute of Aeronautics and Astronautics (AIAA) Paper No. 90-0211, presented at the 28th Aerospace Sciences Meeting, Reno, Nevada, 1990.
[8]J. N. Cuzzi, A. R. Dobrovolskis, and J. M. Champney, "Particle–gas dynamics in the midplane of a protoplanetary nebula," Icarus **106**, 102 (1993).
[9]H. C. Yee, "A class of high-resolution explicit and implicit shock-capturing methods," NASA Technical Memorandum 101088, 1989.
[10]R. W. MacCormack, "The effect of viscosity in high-velocity impact cratering," AIAA Paper No. 69-354, presented at the AIAA Hypervelocity Conference, Cincinnati, Ohio, 30 April–2 May 1969.
[11]L. R. Mendez-Numnez and J. J. Carroll, "Comparison of leapfrog, Smolarkiewicz, and MacCormack schemes applied to nonlinear equations," Mon. Weather Rev. **121**, 565 (1993).
[12]L. R. Mendez-Numnez and J. J. Carroll, "Application of the MacCormack scheme to atmospheric nonhydrostatic models," Mon. Weather Rev. **122**, 984 (1994).
[13]O. B. Toon, R. P. Turco, D. Westphal, R. Malone, and M. S. Liu, "A multidimensional model for aerosols: Description of computational analogs," J. Atmos. Sci. **45**, 2123 (1988).
[14]Y. Nakagawa, M. Sekiya, and C. Hayashi, "Settling and growth of particles in a laminar phase of a low-mass solar nebula," Icarus **67**, 375 (1986).